



HAL
open science

Trail in the atmosphere of the 29 December 2000 meteor as recorded in Tahiti: Characteristics and trajectory reconstitution

A. Le Pichon, Jean Guerin, E. Blanc, D. Reymond

► To cite this version:

A. Le Pichon, Jean Guerin, E. Blanc, D. Reymond. Trail in the atmosphere of the 29 December 2000 meteor as recorded in Tahiti: Characteristics and trajectory reconstitution. *Journal of Geophysical Research: Atmospheres*, 2002, 107, pp.4709. 10.1029/2001JD001283 . hal-03801091

HAL Id: hal-03801091

<https://hal.science/hal-03801091>

Submitted on 14 Oct 2022

HAL is a multi-disciplinary open access archive for the deposit and dissemination of scientific research documents, whether they are published or not. The documents may come from teaching and research institutions in France or abroad, or from public or private research centers.

L'archive ouverte pluridisciplinaire **HAL**, est destinée au dépôt et à la diffusion de documents scientifiques de niveau recherche, publiés ou non, émanant des établissements d'enseignement et de recherche français ou étrangers, des laboratoires publics ou privés.

Copyright

Trail in the atmosphere of the 29 December 2000 meteor as recorded in Tahiti: Characteristics and trajectory reconstitution

A. Le Pichon, J. M. Guérin, and E. Blanc

Commissariat à l'Energie Atomique, Centre DAM - Ile de France, Département Analyse et Surveillance de l'Environnement, Bruyères-le-Châtel, France

D. Reymond

Commissariat à l'Energie Atomique, Laboratoire de Géophysique de Pamatai, Tahiti, French Polynesia

Received 7 September 2001; revised 20 February 2002; accepted 25 February 2002; published 11 December 2002.

[1] On 29 December 2000, a meteor entry in the atmosphere produced several bright lights in the sky of Tahiti and intense sonic booms around midnight local time. This event was detected by the Laboratoire de Détection et de Géophysique French Polynesian seismic network and by the IS24 infrasound station in Tahiti operating for the Comprehensive Test Ban Treaty Organization (CTBTO). Both seismic and infrasonic signals indicated that the altitude of the meteor's last explosion was ~ 45 km. From the wave azimuth and incidence angle determined through infrasonic data processing, the meteor trajectory has been backtracked over 55 km. Determination of the azimuth and incidence angle of the infrasonic arrivals permitted the determination of a 55 km segment of the meteor trajectory. The velocity of the meteor decreased from 17 to 15 km/s in ~ 4 s, while its altitude changed from 55 to 45 km. The diameter and the kinetic energy of the bolide are evaluated using the infrasonic measurements and numerical simulations. *INDEX TERMS:* 0342 Atmospheric Composition and Structure: Middle atmosphere—energy deposition; 1630 Global Change: Impact phenomena; 3384 Meteorology and Atmospheric Dynamics: Waves and tides; 3362 Meteorology and Atmospheric Dynamics: Stratosphere/troposphere interactions

Citation: Le Pichon, A., J. M. Guérin, E. Blanc, and D. Reymond, Trail in the atmosphere of the 29 December 2000 meteor as recorded in Tahiti: Characteristics and trajectory reconstitution, *J. Geophys. Res.*, 107(D23), 4709, doi:10.1029/2001JD001283, 2002.

1. Introduction

[2] The entry of meteors in the atmosphere generates atmospheric waves observed over large distances. In most instances, meteors explode when they penetrate in the upper atmosphere at altitudes of about 70 to 110 km. Larger meteors penetrate deeper into the atmosphere. A blast wave is formed by a rapidly moving point source, which may be conceived as a line source explosion. Although very large events such as the Tunguska meteor can generate low frequency gravity waves, most of the meteors excite acoustic waves in the infrasound domain [ReVelle *et al.*, 1998]. Such infrasounds are refracted and channeled over long distances by the temperature gradient and the wind structure of the atmosphere [Blanc, 1985]. The occurrence of meteor explosions may be observed a few thousand kilometers away from the explosion point. Some of the resulting waves may be Lamb waves guided near the Earth's surface [Francis, 1975]. Detection at shorter distances may give indications about the trail and some of the meteor characteristics.

[3] The implementation of the International Monitoring System (IMS) for the enforcement of the Comprehensive

Nuclear-Test ban Treaty (CTBT) increases the interest in the identification and analysis of explosive bolide events. The global network, which includes radionuclide, hydroacoustic, seismic and infrasound stations, has been designed to detect and locate underground or atmospheric nuclear explosions. Very few meteors reach the ground and generate signals that may be recorded. One event of this kind every few years is expected. Even when recorded, the signals may not allow discrimination between natural events and man-made events [Chyba *et al.*, 1998]. When compared with high altitude nuclear explosions, the number of meteors with an equivalent explosive energy in the range of few kt is ~ 10 per year [Toon *et al.*, 1997; Chyba *et al.*, 1998]. The global infrasound CTBTO network, composed of 60 stations with observation distances reaching few thousands of kilometers, is likely to detect most large bolide explosions. Different methods have been previously used to estimate of the height and the kinetic energy of meteors at different observation distances [Brown *et al.*, 1996; ReVelle and Whitaker, 1996; Evers and Haak, 2001]. This paper, supported by high quality data, aims to improve them using numerical simulation.

[4] Several reports described the breaking up of a meteor in the atmosphere above Tahiti (French Polynesia) on December 29, 2000. The explosion led to the recording of infrasonic waves by the network of the Laboratoire de

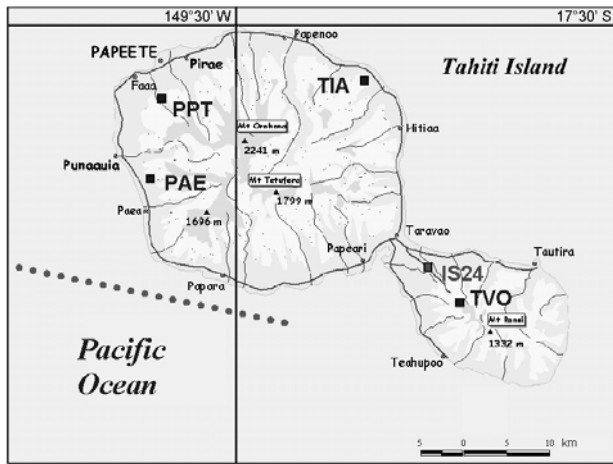


Figure 1. Location of the seismic network (TVO, PAE, PPT, and TIA) and the IS24 infrasound station on Tahiti. The spots indicate the approximate trajectory in the 280–300°N direction according to the pilot’s report.

Détection et de Géophysique (LDG) at Pamatai, composed of seventeen seismometers and the IS24 station that is part of the IMS infrasound network. A detailed analysis of the wave parameter measurements permits the recovery of the meteor trajectory over a distance of several tens of kilometers. The meteor velocity and the incidence angle are determined from the infrasonic measurements. Acoustic models are applied to explain the different wave signatures observed at the different stations. The equivalent explosive energy of the source is estimated by applying a linear source hypothesis [Brown et al., 1996] and using the wave main frequency. A hydrodynamic numerical simulation is carried out to validate this method. This study allows a determination of the meteor diameter and velocity. The detection of meteors at short distances represents an opportunity for a better analysis of meteor entries in the atmosphere while evaluating the IMS efficiency.

2. Visual Observation

[5] On December 29, 2000, several bright lightning illuminated Tahiti around midnight local time (10:00 AM UTC). About two minutes later, a violent explosion was heard on the island. Some reports describe a meteor crossing the sky from west to east and disappearing behind the mountains [Les Nouvelles de Tahiti, 2000]. In his log book, Captain Neil Jones, approaching Papeete on board a of scheduled New-Zealand flight, described the phenomenon in these words [Les Nouvelles de Tahiti, 2000]: “We were about 40 miles south of Tahiti at 12 000 feet when initially we thought there were a couple of flashes. Then we saw a bright light about 20 degrees above our elevation from around 300 degrees magnetic just slightly northwest. We quickly identified it as a meteor. It traveled at right angles to us and descending, and I would say it took about 9 s to pass. I would guess its track would have been about 120 degrees magnetic and looked to be around halfway between Tahiti and us, perhaps 20 miles away. It appeared to be dark in the center, rather than all bright, and had quite some size. We saw a light or halo around the solid center”.

3. Measurements and Wave Parameters

[6] The IS24 station is composed of five microbarometers, 1 to 3 km apart. Each sensor is a MB2000 microbarometer that can measure pressure fluctuations from 0.003 up to 27 Hz. The electronic noise level is 2 mPa RMS in the 0.02–4 Hz frequency band over a dynamic range of 134 dB. The sampling rate is 20 Hz. In order to minimize pressure changes due to surface wind effects, each sensor is connected to an 18-m-diameter noise reducing system equipped with 32 inlet ports. The Polynesian seismic network [Talandier and Okal, 2001] is composed of 17 seismic stations located on different islands. The data of the four seismometers located in Tahiti are used in this study. The other stations located at larger distances from the meteor entry point did not detect any signal. Figure 1 shows the location of the seismic network in Tahiti and the IS24 station.

[7] Figure 2 shows successive wave trains recorded on four microbarometers of IS24 and four seismometers of the seismic network. The signals are complex and variable from one seismometer to another. The first arrival, marked by a vertical line, is assigned to the direct wave generated by the main explosion. Its pressure amplitude is around 0.25 Pa peak-to-peak. The maximum peak-to-peak amplitude of the latter arrivals is about 2 Pa, and most of the energy is in the 0.5–10 Hz band. The waves are also visible on the seismic recordings. The first arrival amplitude measured on the sensors located in the western part of the island (PAE and PPT) is 5 to 10 times greater than the values measured in the eastern part of the island (TVO and TIA). Several coherent wave trains of ~50 s duration are observed at TIA and TVO with waveforms similar to those recorded on the microbarometers.

[8] The wave parameters of the acoustic arrivals measured at IS24 have been calculated with the PMCC method (Progressive MultiChannel Correlation) [Cansi, 1995; Le Pichon et al., 2002]. Figure 3 shows the results of the calculation. Two main wave trains are distinguished, with a lack of detectable coherent signals between 10:06:30 and 10:07:20 UTC. The second wave train amplitude is much

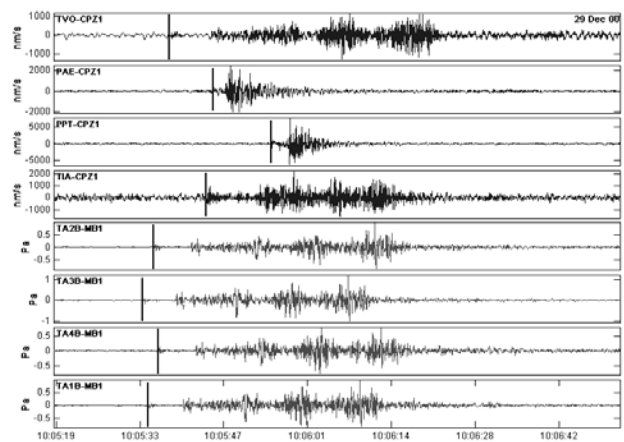


Figure 2. Atmospheric pressure fluctuations recorded on the seismic network (TVO, PAE, PPT, and TIA) and the IS24 station (TA1B, TA2B, TA3B, and TA4B) of Tahiti. Data are filtered from 0.5 to 9 Hz. The vertical lines indicate the arrival times of the first arrival.

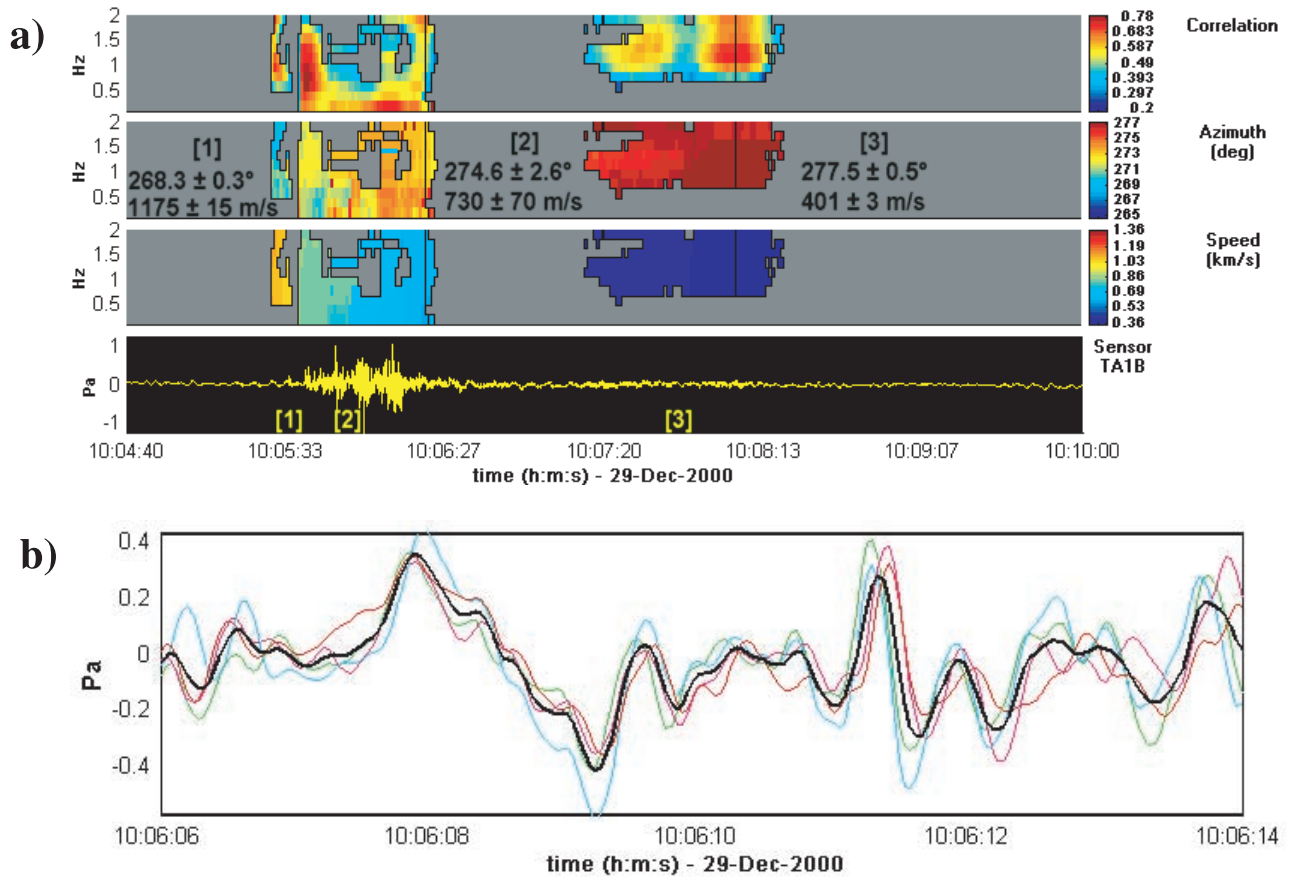


Figure 3. (a) Results of PMCC calculation. The color scales indicate the values of the azimuth and the horizontal trace velocities. Data are filtered from 0.1 to 2 Hz in 10 equally spaced frequency bands. Azimuths are given with respect to the north site. The horizontal trace velocities and azimuths values are indicated for three different arrivals: first arrival [1] picked out in Figure 2, the main wave train [2] and the last phase [3] detected about 2 min after the arrival [1]. (b) Phase-aligned signals (black curve) showing the maximum of energy with a main frequency between 0.3 and 0.8 Hz.

weaker than the first wave amplitude. In both wave trains, the correlation coefficient ranges from 0.42 to 0.76. The velocity decreases with time from 1.17 to 0.40 km/s. As the measured velocity is the apparent horizontal phase velocity, this indicates a decrease of the incidence angle. The azimuth of the first low-amplitude phase is 9° below the mean azimuth of the latter arrivals.

[9] Figure 4 shows the temporal variations of the wave incidence angle β_s (null angle in the horizontal plane) determined assuming that the propagation velocity is the sound speed, and the wave azimuth θ_s . Over a duration of about 170 s, a large variation from 70 to 30° in the incidence angle is observed, while the azimuth changes from 270 to 278° .

4. Meteor Trajectory and Infrasound Propagation

4.1. Reconstitution of the Meteor Trajectory

[10] An analysis of the onset time of the first arrival recorded by the different seismic and infrasound sensors (Figure 2) allows us to locate the meteor explosion. The location is performed using a classical inversion algorithm used in seismology for the determination of the earthquake

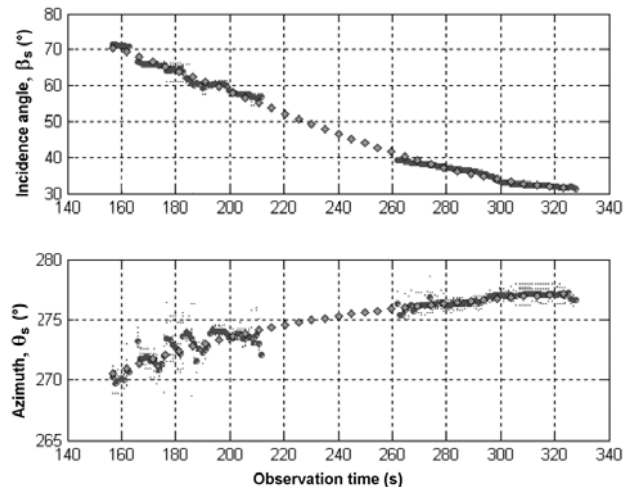


Figure 4. Variations of the incidence angle and the azimuth of coherent wave detected at IS24 versus time. The diamonds represent the complete set of wave parameters as determined by interpolation.

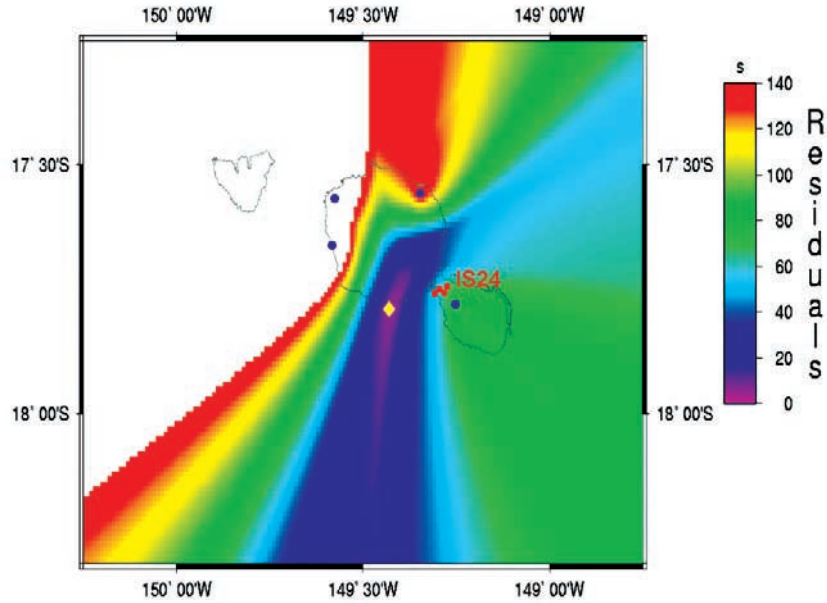


Figure 5. Residuals and location of the last explosion. The grid is covered with a step of 0.01 degrees. The minimum residual is marked in the purple zone with a yellow diamond (17.76°S–149.37°W, altitude: 40–45 km).

depth. The propagation velocity is prescribed in a two-layer model: 340 m/s between 0 and 20 km and 310 m/s above 20 km. The model does not represent the stratospheric sound speed because the explosion height is assumed to be located below the maximum of temperature near 50 km. The incidence angle of the first arrival measured at the infrasound station is also used. This angle is 73° with respect to the horizontal (Figure 4). Figure 5 shows the residual variation of the arrival times for different locations. The explosion hypocenter (17.76°S–140.37°W, altitude range of 40–45 km) corresponds to the minimum residual.

[11] To complement this location, the incidence angle and the azimuth variation versus time (Figure 4) are used to reconstruct the meteor trajectory. As the source is close to the station (less than 50 km), the curvature of acoustic rays is considered negligible. The acoustic propagation path to the station is assumed to be rectilinear with a sound speed velocity C_0 averaged from the ground level to the explosion height. Given these assumptions, a non-linear equation system links the meteor coordinates with respect to the time and to the IS24 station coordinates.

$$\begin{aligned}
 t_s &= t + \frac{\sqrt{(x-x_s)^2 + (y-y_s)^2 + z^2}}{c_0} \\
 z &= Vt \sin(\beta) + z_0 \\
 x^2 + y^2 &= V^2 t^2 \cos^2(\beta) \\
 x^2 + y^2 + (z-z_0)^2 &= V^2 t^2 \\
 \sin(\beta_s) &= \frac{z}{\sqrt{(x-x_s)^2 + (y-y_s)^2 + z^2}} \\
 x_s - x &= \sqrt{(x-x_s)^2 + (y-y_s)^2} \cos(\theta_s)
 \end{aligned}
 \tag{1}$$

The points $M_s(x_s, y_s, 0)$ et $M(x, y, z)$ characterize the IS24 station and the source point, respectively (Figure 6). The variable t represents the time of the wave emission at the source and t_s is the time measured at the infrasound station. The time origin is taken to be at the end of the trajectory at $t = 0$ s, when the M point coordinates are $(0, 0, z_0)$, z_0 being the height of the last explosion (Figure 5). Then $t_s - t$ is the propagation time and equals 155 s. The trajectory incidence angle, β , is measured from the horizontal plane at a height $z = z_0$.

[12] The equation system (1) is solved using an iterative resolution algorithm for non-linear equations [Coleman and Li, 1996]. At each observation point (about 700 triplets $[t_s, \theta_s, \beta_s]$), the coordinates $[x, y, z, t]$ are evaluated after

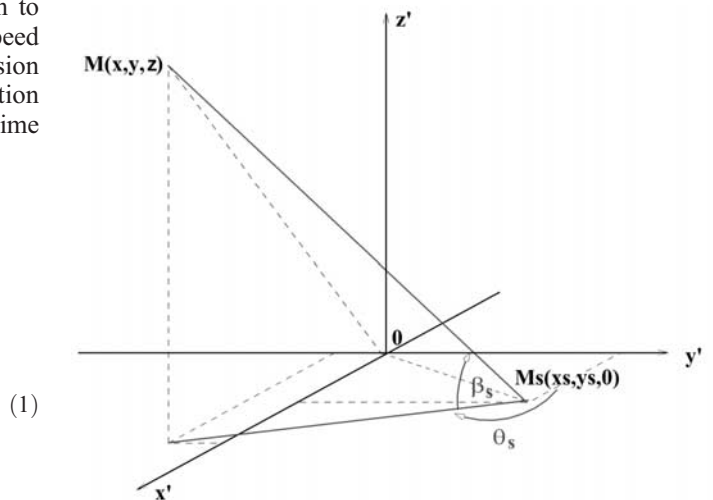


Figure 6. Coordinate system for the meteor trajectory reconstitution.

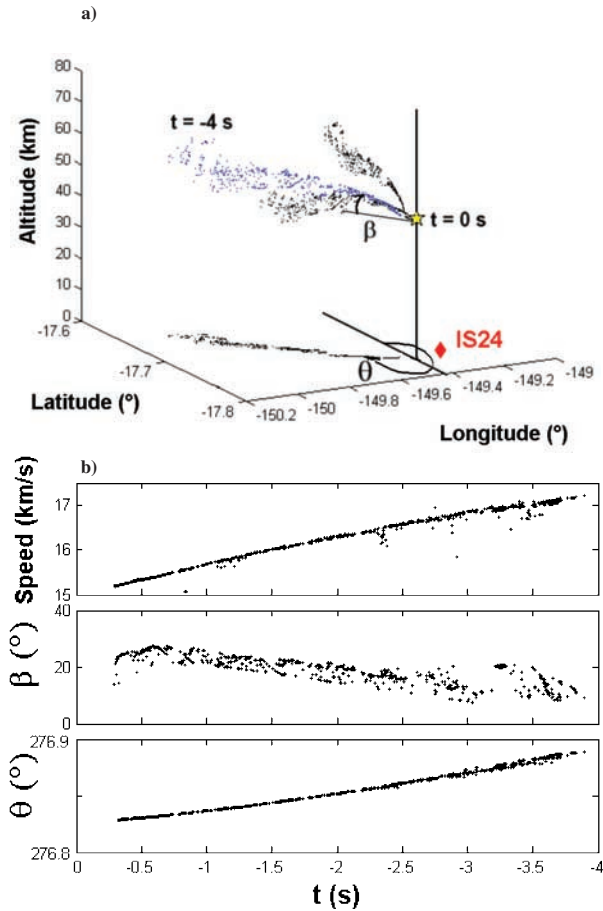


Figure 7. (a) Reconstruction of the meteor trajectory approaching Tahiti based on the azimuth and the wave incidence variations. The blue points indicate the three-dimensional trajectory. The black points show the trajectory projected onto the three planes of the Cartesian reference system. (b) Estimates of velocity, trajectory incidence angle β with respect to the horizon and azimuth θ from the north. The time reference of the meteor is represented by the yellow diamond (location point in Figure 5).

convergence of the calculation (Figure 7). Over a duration of 4 s, the velocity decreases from 17 km/s to 15 km/s with a numerical uncertainty of less than 50 m/s. The trajectory azimuth θ is nearly constant between 276.8 and 276.9°. The trajectory incidence angle β varies from about 25 to 10° while the meteor altitude decreases from 55 to 45 km. The results of this calculation are in agreement with the pilot's statement indicating a meteor trajectory that was fairly horizontal in the 280–300° N direction.

4.2. Propagation Modeling

[13] From the estimated trajectory, ray-tracing simulations are performed in order to explain the differences seen in the waveforms (Figure 2). Numerical simulations are conducted at different times of the trajectory. Ray paths are computed for waves propagating in a stratified atmosphere under the influence of an altitude-dependent wind profile [Garcés *et al.*, 1998, 2002]. The wind and temperature profiles used in the simulations are computed from the

MSISE-90 and HWM-93 empirical reference models [Hedin *et al.*, 1996]. These models involve detailed parameterization of seasonal changes in the mean state of the atmosphere, including dominant solar migrating tides and low-order stationary planetary waves. The empirical models provide time-dependent temperature and composition profiles as well as zonal (W-E) and meridional (S-N) wind estimates up to altitudes of 200 km. These profiles account for the mean effects of seasonal wind reversals above the troposphere and daily solar tide variability in the mesosphere-lower thermosphere. The ray paths are obtained for the atmospheric conditions of December 29, 2000 at 10:00 UTC. To explain the observed signal amplitude variations at each station, we hypothesize that the bolide disintegrated in a series of explosions, which radiated isotropically.

[14] Three source points are chosen: at the hypocenter of the last explosion at $t_0 = 0$ s (17.76°S – 149.37°W, $z = 45$ km), at $t = -0.9$ s (17.73°S – 149.56°W, $z = 49$ km) and at $t_2 = -2.1$ s (17.71°S – 149.74°W, $z = 53$ km). The bounce locations and the acoustic ray traces radiated downward are shown in Figure 8. The pressure variations at one microbarometer and at four seismic sensors, on which the times t_0 , t_1 and t_2 are reported, are presented at the bottom of the figure.

[15] At $t_0 = 0$ s, the stations IS24, TVO, TIA, PAE and PPT are at horizontal distances of 12, 15, 22, 23 and 26 km from the source, respectively. The location of the shadow zone with respect to the seismic and acoustic measurement points allows the analysis of qualitative differences in the direct wave amplitude. As indicated by the green vertical lines on the signals, the amplitude measured at TVO is about four times smaller than at TIA. This can be explained by the different distances between the sensors and the epicenter: TVO is located inside the shadow area, whereas TIA is located on its edge.

[16] At $t_1 = -0.9$ s, the stations IS24, TVO, TIA, PAE and PPT are at horizontal distances of 28, 33, 30, 8 and 18 km from the source, respectively. The red lines on the signals show that the amplitudes measured at PAE and PPT are very weak and close to the background noise level. Only the station IS24 and the seismic sensors TIA and TVO, located on the edge of the shadow zone, record similar signals with larger amplitudes. These differences are explained by the position of PAE and PPT inside the shadow zone.

[17] At $t_2 = -2.1$ s, the stations IS24, TVO, TIA, PAE and PPT are at horizontal distances of 47, 52, 48, 17 and 23 km from the source, respectively. As observed at $t = -0.9$ s, PAE and PPT are still located inside the shadow zone. No signal is apparently observed at TIA and TVO. A greater propagation distance can explain this lack of signal. On the infrasonic recordings, no signal is visible on the raw data but a second wave train is detected by PMCC at 10:07:30 UTC (Figure 3). The low incidence angle (30–40°) of the latter wave train corresponds to a first explosion, later detected at a greater distance because of the supersonic motion of the source.

5. Size and Energy Estimation

[18] Using a drastic simplification, a massive body penetrating the atmosphere, with a velocity considerably greater

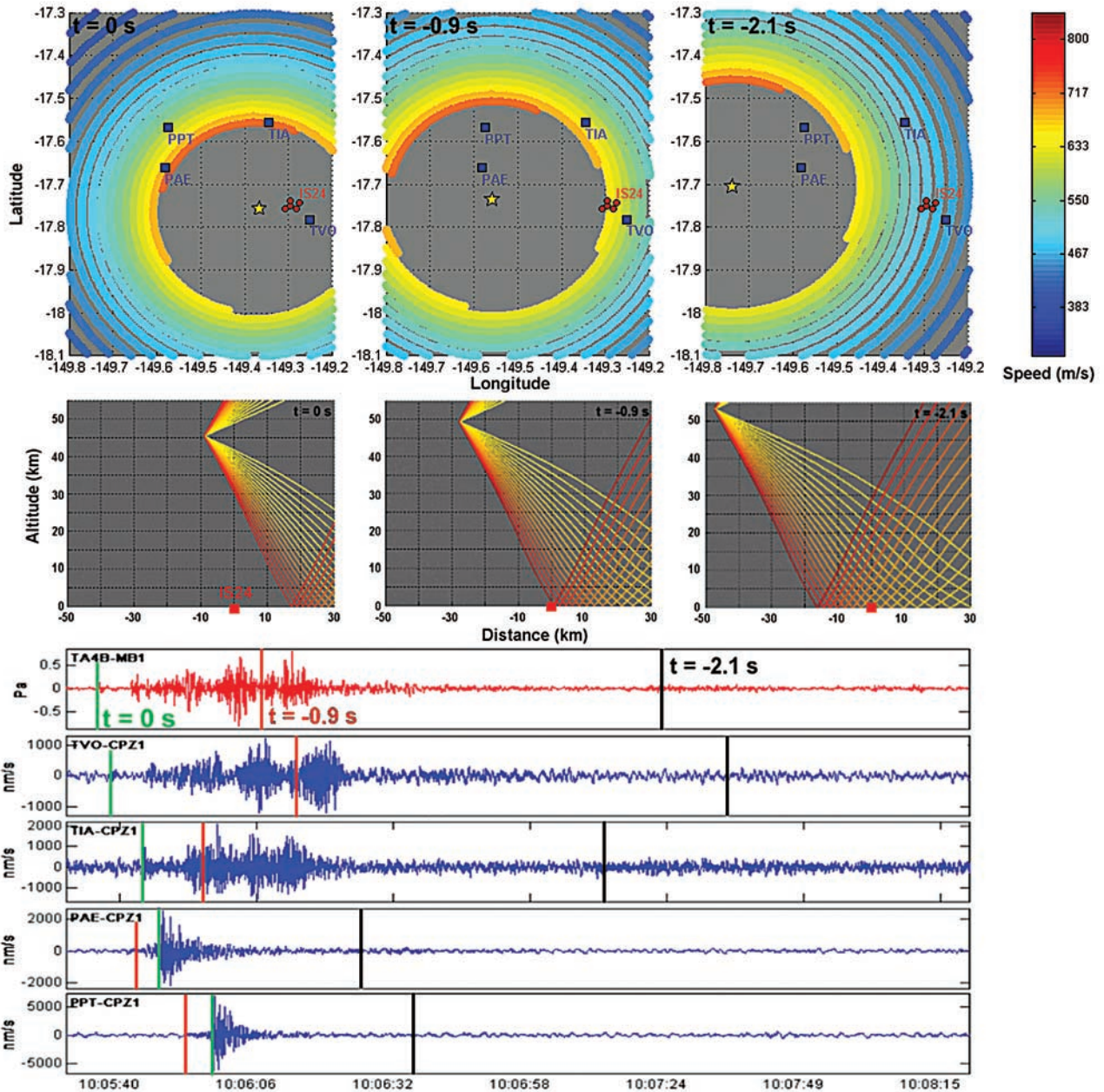


Figure 8. Ray-tracing simulation. (top) Bounce locations of the acoustic rays. The color indicates the corresponding horizontal speed value. (middle) Acoustic ray paths from the explosion point at $t = 0$ s, -0.9 s and -2.1 s. The radius of the shadow zone is 26, 28 and 30 km, respectively. (bottom) Recordings on the seismic network and the infrasound sensors. The vertical lines indicate the arrival times of the waves at the different sensors.

than the speed of sound, instantaneously loses a large part of its kinetic energy and thus generates a shock wave in the medium. It suffers such a strong deceleration that it is fragmented before reaching the ground surface. The shock wave generation associated with this penetration leads to the production of a pressure wave whose main frequency is related to the size and the velocity of the meteor.

[19] The diameter and kinetic energy of a meteor are obtained from the fundamental frequency identified from the first observed coherent wave. The blast wave model is presented and discussed in the first part of this section. The

meteor parameters are deduced from this model in the second part. The explosive energy is calculated from an empirical analysis in a third part.

5.1. Description and Evaluation of the Meteor Blast Wave Model

[20] The model usually employed to describe the meteor blast wave assumes a linear source as introduced by *Lin* [1954]. As it enters the atmosphere, the meteor creates a cylindrical pattern of energy release, which is considered to be the source of the infrasonic signal. The cylindrical blast

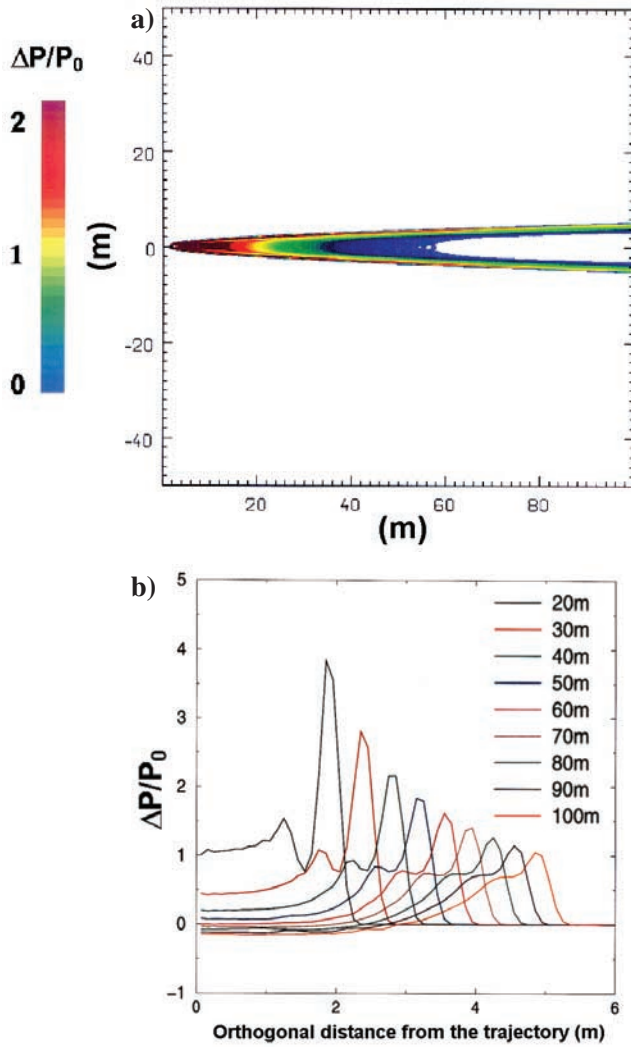


Figure 9. Eulerian finite difference hydro-code simulation of a meteor penetrating into the atmosphere at a height of 50 km. The meteor has a 30-cm diameter with a relative velocity in the fluid of 15 km/s. (a) Multilevel curves of $\Delta P/P_0$ at a particular time. (b) Superposition of the $\Delta P/P_0$ simulated profile curves as computed on the left. The cross-sections are taken at distances ranging from 20 m to 100 m along the trajectory axis.

wave radius R_0 was first introduced by *Tsikulin* [1970] and was computed by *ReVelle* [1976]. This radius is defined as the radial distance between the meteor propagation axis and the point where the generated overpressure propagates at a linear rate. This hypothesis is expressed in terms of the following condition:

$$\frac{\Delta P}{P_0} = \frac{p(R_0) - p_0(z)}{p_0(z)} = 1 \quad (2)$$

where $p(R_0)$ represents the shock wave pressure produced in the media and $p_0(z)$ is the ambient pressure depending on height, z .

[21] In addition, the shock wave formation takes place only if the Mach number is greater than unity and if the

object dimension is much greater than the mean free path of the air molecules in the atmospheric layer. Under this condition, the R_0 parameter is roughly of the same order than the product of the Mach number and the object diameter:

$$R_0 = M_a \phi \quad (3)$$

where M_a is the Mach number (ratio V/C_s between the object velocity V and the sound speed C_s) and ϕ its initial diameter before ablation.

[22] The first condition is approximately satisfied at usual meteor speeds (usually greater than 10 km/s) for an object of meter-scale dimensions, while the second condition is fulfilled at an altitude of 100 km where the mean molecular free path is around 1 m (U.S. Standard Atmosphere, 1976). R_0 is determined by a hydrodynamic numerical simulation that computes the overpressure generated in the meteor tail (Figure 9). The meteor trajectory is simulated with an Eulerian finite difference hydro-code that applies a fast airflow around an iron sphere. The initial pressure and density conditions are those prevailing at an altitude of 50 km: air density of 0.01 kg/m^3 , atmospheric pressure of 100 Pa [U.S. Standard Atmosphere, 1976]. The calculation grid is regular and fitted to the object size. In this approach, R_0 represents the radius of the shock elastic area. In this simplified calculation, the material ablation and the meteor deceleration are taken into account. The boundary conditions are opened in order to simulate an outflow in an infinite medium and to maintain an undisturbed established flow. Figure 9 shows multilevel curves of $\Delta P/P_0$ obtained by numerical simulations.

[23] Figure 10 shows a comparison between the simulation performed by *ReVelle* [1976] and the results of the simulation. Figure 10 presents the maximum overpressure versus the radial distance divided by $M_a \phi$. The black arrow indicates the evaluation of R_0 in the particular case of a 30-

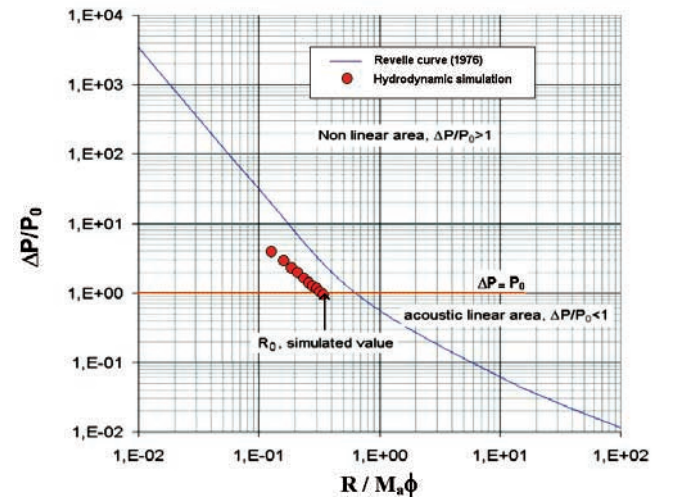


Figure 10. Relative overpressure versus reduced distance with respect to the product $M_a \phi$ in a homogeneous atmosphere. Superimposition of the *ReVelle* curve [1976] and the simulation results for a 30-cm diameter object at Mach 50.

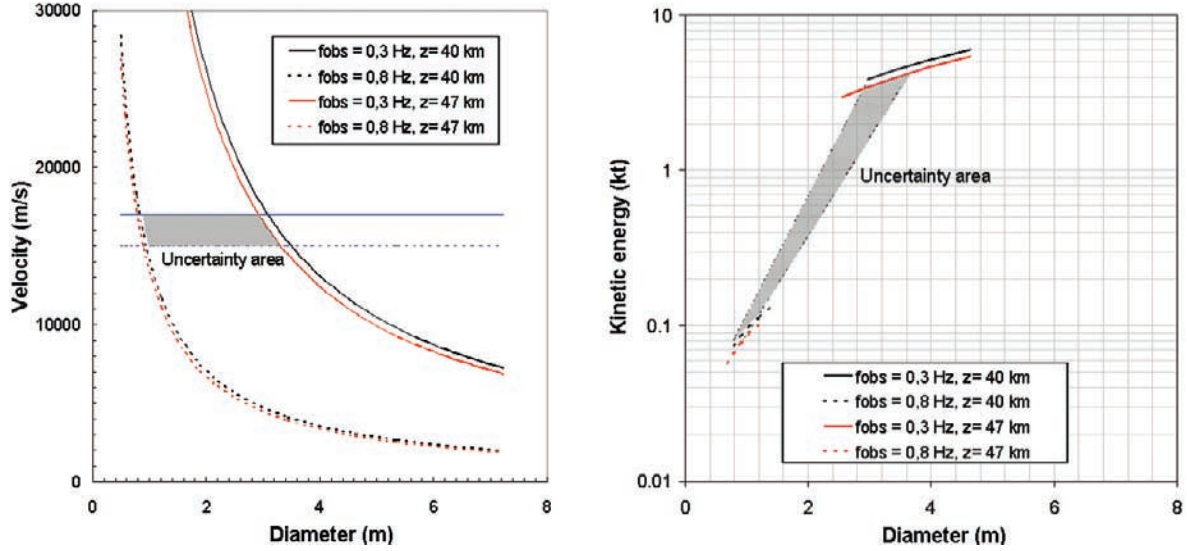


Figure 11. Upper bounds for the size and the kinetic energy of the meteor. Left: Probable solution in the velocity/diameter domain. The horizontal lines show the velocity range deduced from signal analysis (Figure 7). Right: Same solution range in the kinetic energy/diameter domain assuming a density of 7500 kg/m³.

cm-diameter object penetrating the atmosphere at a velocity of Mach 50. Derived from this simulation, R_0 is close to $0.35 M_a \phi$. This smaller value can be an effect of the numerical viscosity parameters required by finite difference methods [Wilkins, 1980].

[24] This result is now compared with the original linear source model. In his paper, Lin [1954] demonstrates a general relation between the cylindrical shock wave pressure $p(R)$, the radial distance R and the energy released per unit length E :

$$P(R) = 0.216 E/R^2 \quad (4)$$

Assuming that $E = F E_k/L$, where E_k is the total kinetic energy, L the source cylinder length and F a coupling factor less than 1, the previous equation becomes:

$$P(R) = 0.216 \frac{F E_k}{L R^2} \quad (5)$$

Using the previous expression of the Mach number and assuming that the air is a perfect gas with constant ratio of specific heats $\gamma = 1.4$, equation (5) becomes:

$$P(R) = \frac{0.216 \pi \gamma}{12} \frac{F \varphi^3 M_a^2}{L R^2} \frac{\rho}{\rho_0} \quad (6)$$

where ρ and ρ_0 are the meteor and the air density, respectively. Substituting this expression into equation (2) and assuming a coupling factor $F < 1$, it becomes:

$$R_0 < \sqrt{\frac{0.216 \pi \gamma}{24} \frac{\rho}{\rho_0} \frac{\varphi}{L} M_a \varphi} \approx 0.2 \sqrt{\frac{\rho}{\rho_0} \frac{\varphi}{L} M_a \varphi} \quad (7)$$

The product is then evaluated with the example of a meteor of $\phi = 1$ m with a metallic density crossing the half atmosphere from 50 km high. With a local mean density

around $5 \cdot 10^{-2}$ kg/m³, it becomes $R_0 < 0.4 M_a \phi$. The results obtained with the relations $R_0 = M_a \phi$ and $R_0 < 0.4 M_a \phi$ will be discussed hereafter.

5.2. Determination of the Meteor Diameter and Kinetic Energy

[25] ReVelle and Whitaker [1996] have established that the dominant wave frequency in a region with sound speed C_s near the source (evaluated approximately at 10 times the R_0 distance) is obtained from the equation:

$$f = \frac{C_s}{2.81 R_0} \quad (8)$$

Due to dispersal effects, at a distance R from the meteor propagation axis and in the 1–5 Hz band, the main frequency at ground level becomes the ground-observed frequency f_{obs} :

$$f_{obs} = 1.78 f \left(\frac{R_0}{R} \right)^{\frac{1}{4}} \quad (9)$$

The main frequency, the radial distance R and the ratio velocity/mass or velocity/diameter are obtained from ground observations. The velocity is expressed without R_0 using the equations (3), (8), and (9)

$$V = \frac{C_s}{\Phi} \left(0.63 \frac{C_s}{f_{obs} R^{\frac{1}{4}}} \right)^{\frac{4}{3}} \quad (10)$$

The kinetic energy E_k represents an upper limit to the explosive energy of an equivalent TNT charge,

$$E_k = \frac{1}{2} \rho \left(\frac{\pi \Phi^3}{6} \right) V^2 \quad (11)$$

Figure 11 presents upper bound estimates for the diameter and the kinetic energy of the meteor with a velocity between 15 km/s and 17 km/s (Figure 7), a density similar to that of iron (7500 kg/m³), a radial distance R of 50 km (range of 12 km and height of 40–45 km), and a measured frequency of 0.3–0.8 Hz (Figure 3). The parameter R_0 is obtained from equation (9) as a function of the measured frequency f_{obs} . The solution domain can be visualized by plotting the meteor velocity versus its diameter for different frequencies and altitudes (Figure 11). The uncertainty area is large but the use of the measured meteor velocity (15–17 km/s) improves the accuracy of the estimate. A diameter from 0.70 to 3.50 m is obtained, leading to an equivalent TNT mass between 1.5 tons and 150 tons. The corresponding kinetic energy ranges from 60 tons to 4 kilotons. It is noteworthy that the main source of uncertainty is due to the determination of the frequency. Since only objects of diameter greater than one meter are able to touch down [Brown *et al.*, 1996], and according to the visual observations of the pilot, the kinetic energy should be greater than 100 tons.

[26] Using the formula $R_0 < 0.4 M_a \phi$, the range of values taken by the meteor diameter and the energy kinetic are reevaluated. The diameter and the energy kinetic reach 8 m and 90 kt, respectively. This second evaluation yields to larger ranges compared to the results obtained with the equation $R_0 = M_a \phi$.

5.3. Determination of the Explosive Energy

[27] The energy of an equivalent TNT explosion represents the explosive charge, which involves the same effects as the shock induced by the meteor penetrating through the atmosphere. It can be empirically evaluated by comparing its effects with those of low-altitude nuclear explosions using the following relation [Whitaker and ReVelle, 1995]:

$$\log_{10}(E_s/2) = 3.34 \log_{10}\left(\frac{1}{f_{obs}}\right) - 2.58 \quad (12)$$

where E_s represents the energy of an equivalent TNT explosion and is limited to $E_s < 100$ kt. This relation leads to an equivalent TNT mass ranging from 10 t to 300 t. This evaluation is compatible with the kinetic energy previously calculated.

6. Conclusion

[28] Infrasonic waves generated by a meteor explosion over Tahiti (French Polynesia) on December 29, 2000, were measured on four seismic sensors of the Polynesian network and on the IS24 station belonging to the IMS. Numerous statements reported a violent explosion lighting up the sky and the fall of a voluminous object.

[29] An analysis of the seismic and acoustic recordings shows the presence of several wave trains characterized at the local scale by very different phase velocities, azimuths and amplitudes. The location of the last explosion is obtained with a residual close to 1 second. This location corresponds to a hypocenter situated at 13 km from the central point of the infrasound station and at a height of 40–45 km. A detailed analysis of the wave parameters allows a reconstruction of the meteor trajectory over a distance of

~55 km, corroborating the observations. The velocity of the meteor varies from 17 to 15 km/s during ~4 s while the altitude changes from 55 to 45 km. Simulated wave propagation from several trajectory points also explains the different observed phases and differences in amplitude from one sensor to another.

[30] The non-linear propagation radius, R_0 , is a characteristic length of the infrasonic source. Usually approximated by the product between the meteor diameter and the Mach number, R_0 can be derived from the main signal frequency (0.3 Hz–0.8 Hz). A diameter of 0.70 to 3.50 m is deduced from published scaling relationships. With a mean density close to that of iron, the meteor would have a mass between 1.5 t and 150 t and a kinetic energy of 100 t to 4 kt. A numerical evaluation of R_0 has been also performed with a combination of a finite difference hydro-code and analytical developments. It leads to a lower estimation of R_0 , which induces a greater size up to 8 m and a higher meteor kinetic energy. According to the pilot's report of a touchdown in the sea, it appears that the greater size hypothesis should be favored. The explosive energy is estimated to be between 10 t and 300 t.

[31] This work applies to a natural event various technical and analytical detection methods developed with the aim of monitoring the CTBT. It demonstrates the importance of seismo-acoustic synergy to obtain the precise location of a moving source. Finally, it shows the usefulness of acoustic wave simulations in explaining waveforms that may exhibit significant signature discrepancies from one sensor to the other. The expected number of events similar to the Tahiti meteor, is about 100 per year [Toon *et al.*, 1997]. From the present study and the spatial distribution of the French Polynesia miniarray, the detection range is evaluated to be about 200 km. Since the CTBTO infrasound stations are multisensor stations, the use of a correlation-based method adapted for the analysis of low-amplitude coherent waves could increase this detection range. Applied to the 60 stations of the CTBTO, a detection range of 200 km gives a minimum observation frequency of 1 to 2 meteors per year and per station. Meteor entry evidences would probably occur more frequently in the next years because of the increasing number of stations. Because of new numerical simulation capabilities, our knowledge of meteor characteristics and trajectories in the atmosphere will improve over time.

[32] **Acknowledgments.** The authors gratefully thank Captain Neil Jones for his precise description, and the time he spent helping us. They also thank Dr. J.L. Plantet for his contribution to the source location technique. Many thanks to Milton Garcés for his detailed review of the original manuscript and his consultations on infrasonic propagation.

References

- Blanc, E., Observations in the upper atmosphere of infrasonic waves from natural or artificial sources: A summary, *Ann. Geophys.*, 3, 673–687, 1985.
- Brown, P., A. R. Hildebrand, D. Green, D. Pagé, C. Jacobs, D. O. ReVelle, E. Tagliaferri, J. Wacker, and B. Wetmiller, The fall of the St-Robert meteorite, *J. Meteoritics Planet. Sci.*, 31, 502–517, 1996.
- Cansi, Y., An automatic seismic event processing for detection and location: The PMCC method, *Geophys. Res. Lett.*, 22, 1021–1024, 1995.
- Chyba, C. F., G. E. Van Der Vink, and C. B. Hennes, Monitoring the Comprehensive Test Ban Treaty: Possible ambiguities due to meteorite impacts, *Geophys. Res. Lett.*, 25(2), 191–194, 1998.
- Coleman, T. F., and Y. Li, An interior, trust region approach for nonlinear minimization subject to bounds, *SIAM J. Optim.*, 6, 418–445, 1996.

- Evers, L. G., and H. W. Haak, Listening to sounds from an exploding meteor and oceanic waves, *Geophys. Res. Lett.*, 2, 41–44, 2001.
- Francis, S. H., Global propagation of atmospheric gravity waves: A review, *J. Atmos. Sol. Terr. Phys.*, 37, 1011–1054, 1975.
- Garcés, M., R. A. Hansen, and K. G. Lindquist, Travel times for infrasonic waves propagating in a stratified atmosphere, *Geophys. J. Int.*, 135, 255–263, 1998.
- Garcés, M., D. P. Drob, and J. M. Picone, A theoretical study of the effect of geomagnetic fluctuations and solar tides on the propagation of infrasonic waves in the upper atmosphere, *Geophys. J. Int.*, 148, 77–87, 2002.
- Hedin, A. E., et al., Revised global model of upper thermospheric winds using satellite and ground-based observations, *J. Geophys. Res.*, 96, 7657–7688, 1996.
- Le Pichon, A., M. Garcés, E. Blanc, M. Barthélémy, and D. P. Drob, Acoustic propagation and atmosphere characteristics derived from infrasonic waves generated by the Concorde, *J. Acoust. Soc. Am.*, 111, 629–641, 2002.
- Les Nouvelles de Tahiti, Une météorite explose au-dessus de Tahiti, Paapeete, Tahiti, 2000.
- Lin, S., Cylindrical shock waves produced by an instantaneous energy release, *J. Appl. Phys.*, 25, 54–57, 1954.
- ReVelle, D. O., On meteor-generated infrasound, *J. Geophys. Res.*, 81, 1217–1230, 1976.
- ReVelle, D. O., and R. W. Whitaker, Detection of large meteoroid/NEO flux using infrasound recent detection of the November 21, 1995 Colorado fireball, *Los Alamos Natl. Lab. Rep.*, LA-UR-96-2236, Los Alamos Natl. Lab., Los Alamos, N.M., 1996.
- ReVelle, D. O., R. W. Whitaker, and W. T. Armstrong, Infrasound from the El Paso Super-bolide of October 9, 1997, in *SPIE Conference on Characteristics and Consequences of Space Debris and Near-Earth Objects*, Int. Soc. for Opt. Eng., Bellingham, Wash., 1998.
- Talandier, J., and E. A. Okal, Identification criteria for sources of T-waves recorded in French Polynesia, *Pure Appl. Geophys.*, 158, 567–603, 2001.
- Toon, O. B., R. P. Turco, and C. Covey, Environmental perturbations caused by the impacts of asteroids and comets, *Rev. Geophys.*, 35(1), 41–78, 1997.
- Tsikulin, M., Shock waves during the movement of large meteorites in the atmosphere, *Tech. Rep.*, AD 715-537, Natl. Tech. Inform. Serv., Springfield, Va., 1970.
- Whitaker, R. W., and D. O. ReVelle, Analysis of the acoustic conversion efficiency for infrasound from atmospheric entry of NEO's, *Los Alamos Natl. Lab. Rep.*, LA-UR-95-4121, Los Alamos Natl. Lab., Los Alamos, N.M., 1995.
- Wilkins, M. L., Use of artificial viscosity in multidimensional fluid dynamic calculation, in *Fluid Dynamics Calculations*, *J. Comput. Phys.*, 36, 281–303, 1980.
-
- E. Blanc, J. M. Guérin, and A. Le Pichon, Commissariat à l'Energie Atomique, Centre DAM - Ile de France, Département Analyse et Surveillance de l'Environnement, BP 12, 91680 Bruyères-le-Châtel, France. (lepichon@dase.bruyeres.cea.fr)
- D. Reymond, Commissariat à l'Energie Atomique, Laboratoire de Géophysique de Pamatai, Tahiti, French Polynesia.